

An n -th order Lagrangian Forward Model for Large-Scale Structure

Fabian Schmidt^a

^aMax-Planck-Institut für Astrophysik, Karl-Schwarzschild-Straße 1, 85748 Garching, Germany

E-mail: fabians@mpa-garching.mpg.de

Abstract. A forward model of matter and biased tracers at arbitrary order in Lagrangian perturbation theory (LPT) is presented. The forward model contains the complete LPT displacement field at any given order in perturbations, as well as all relevant bias operators at that order and leading order in derivatives. The construction is done for any expansion history and does not rely on the Einstein-de Sitter approximation. A large subset of higher-derivative bias operators is also included. As validation test, we compare the n LPT-predicted matter density field and that from N-body simulations using the same initial conditions. For simulations using a cutoff in the initial conditions, we find subpercent agreement up to scales of $k \sim 0.2 h^{-1} \text{Mpc}$. We also find subpercent agreement with full simulations without cutoff, both for the power spectrum and nonlinear σ_8 -inference, when allowing for the effective sound speed. The application to biased tracers (halos) has already been presented in a recent paper [1].

Keywords: cosmological parameters from LSS, redshift surveys, dark matter halos, bias, effective field theory

ArXiv ePrint: [2012.09837](https://arxiv.org/abs/2012.09837)

Contents

1	Introduction	1
2	Lagrangian perturbation theory	2
3	Bias expansion at leading order in derivatives	6
4	Higher-derivative bias	8
5	Numerical implementation	9
6	Comparison with N-body simulations	10
6.1	Simulations with cutoff	11
6.2	Full simulations	13
6.3	Profile likelihood for σ_8	16
7	Conclusions	17
A	Einstein-de Sitter solution of LPT	18
B	Transverse contributions to LPT source terms	19

1 Introduction

A *forward model* of large-scale structure (LSS) evolves a given set of initial conditions—in the form of a linear matter density field used to initialize the growing mode of structure formation—into the observed structure today. The latter can consist of the total matter density field, as probed in projected form via gravitational lensing, or the density field of biased tracers, as observable using galaxy surveys. Such forward models can be used for a variety of purposes: to construct mock observations (see [2] and references therein); to reduce sample variance in the comparison to full simulation results [3–7]; to provide an alternative means to predict summary statistics of the observables such as power spectra and three-point functions (bispectra) and their covariance [2, 8, 9]; and for use in full Bayesian inference approaches, where such forward models provide a prediction for the mode of the field-level likelihood for given initial conditions [10–14].

One well-known forward model of LSS consists in N-body simulations, which fully non-linearly solve for the evolution of cold collisionless matter under gravity. Apart from the fact that full simulations are very costly, however, perturbative forward models (see [15] for a review of perturbative approaches to LSS) are well motivated by the fact that they allow us to rigorously incorporate non-gravitational small-scale physics, including baryonic feedback, via free bias coefficients (see [16] for a review). This allows them to be applied to the case of biased tracers, whose formation cannot be simulated realistically in general.

In perturbative forward models, one can take either the Eulerian [8] or Lagrangian route [4, 17, 18]. However, none of the existing published forward models include the general bias expansion beyond second order. The forward model presented here aims to add precisely that. In addition, it also computes the perturbation theory solutions as well as general bias

expansion for a general expansion history (see also [19, 20]), rather than the Einstein-de Sitter approximation assumed in the published perturbative forward models.

The forward model presented here is based on Lagrangian perturbation theory (LPT), which has been studied extensively for matter [4, 21–26], but also for biased tracers [27, 28]. There are several strong reasons for using a Lagrangian formulation for LSS forward models:

1. The LPT prediction shows a much better correlation with the fully nonlinear evolved density field than Eulerian perturbation theory (e.g., [3, 29]).
2. The general bias expansion described in [16, 30] can be implemented in a straightforward way based on n -th order LPT. In the Eulerian case, this expansion is much more complicated due to the convective time derivatives involved.
3. Performing the bias expansion first before displacing to the Eulerian position allows for the simple incorporation of redshift-space distortions and lightcone effects (not discussed here in detail, but see [18, 31] and Sec. 7).

The general bias expansion, which at any given spacetime location incorporates the density and tidal field along the past trajectory, is an expansion in orders of perturbations and derivatives. As mentioned above, the Lagrangian forward model generates all bias terms up to any given order in LPT, but at leading order in derivatives. A corresponding expansion up to any order in derivatives is technically challenging due to memory requirements and the difficulty in removing degeneracies between different operators. However, we describe here how to systematically construct a non-degenerate subset of higher-derivative operators.

The main goal of this paper is to present the forward model and validate it by comparing the resulting matter density field to that obtained in full N-body simulations. We also employ N-body simulations that start from initial conditions with a sharp- k filter, setting all initial perturbations with $|\mathbf{k}| > \Lambda$ to zero. This allows for precise comparisons in the regime where the entire density field remains under perturbative control.

The application to biased tracers has already been presented in [1], based on [32]. Specifically, that paper studied the inference of the amplitude of primordial fluctuations from halos in N-body simulations using the field-level likelihood based on the effective field theory [13, 33–35]. In that case, the complete bias expansion including higher-derivative terms described here was employed. For sufficiently small values of the cutoff Λ , convergence to an unbiased estimate was demonstrated. However, many more tests on biased tracers, including comparing correlation functions, could be done.

The outline of the paper is as follows: Sec. 2 reviews the LPT construction. We then turn to the general bias expansion in Sec. 3 as well as its extension to higher derivatives in Sec. 4. The numerical implementation is described in Sec. 5. We then present results in Sec. 6 and conclude in Sec. 7. The appendices give more details on the LPT solution.

2 Lagrangian perturbation theory

Lagrangian perturbation theory starts with the geodesic equation for nonrelativistic matter with initially vanishing peculiar velocity and density perturbation. We write the spatial part of the solution of this equation of motion as

$$\mathbf{x}_\text{fl}(\mathbf{q}, \tau) = \mathbf{q} + \mathbf{s}(\mathbf{q}, \tau), \quad (2.1)$$

where $\mathbf{s}(\mathbf{q}, \tau)$ is the Lagrangian displacement, with $\lim_{\tau \rightarrow 0} \mathbf{s}(\mathbf{q}, \tau) = 0$, and \mathbf{q} is the Lagrangian coordinate \mathbf{q} . Then, the equation for the displacement \mathbf{s} is given by

$$\mathbf{s}''(\mathbf{q}, \tau) + \mathcal{H}\mathbf{s}'(\mathbf{q}, \tau) = -\nabla_x \Phi(\mathbf{x}, \tau) \Big|_{\mathbf{x}=\mathbf{q}+\mathbf{s}(\mathbf{q}, \tau)}, \quad (2.2)$$

where primes denote derivatives with respect to conformal time τ . The initial conditions are set at very early times $\tau \rightarrow 0^+$ by setting \mathbf{s}, \mathbf{s}' to a purely longitudinal, growing-mode linear displacement field and its time derivative, as we will describe below. The system is closed via the Poisson equation

$$\nabla_x^2 \Phi(\mathbf{x}, \tau) = \frac{3}{2} \Omega_m(\tau) \mathcal{H}^2(\tau) \delta(\mathbf{x}, \tau). \quad (2.3)$$

Specifically, we work with a metric in conformal-Newtonian gauge, and with the matter density defined in synchronous-comoving gauge, so that a fixed τ slice corresponds to fixed proper time for comoving observers. With these definitions, Eq. (2.3) remains valid on all scales (see Sec. 2.9 of [16] and references therein). Relativistic corrections then only need to be applied when connecting quantities defined on proper-time slices to measurements made by a distant observer through light signals (see [36] for a review).

Notice further that any scale-independent modification of the linear Poisson equation, due to a modification of gravity for example, can be incorporated in the following by absorbing the modification into a redefined $\Omega_m(\tau)$.

Two further relations are needed. First, from Eq. (2.1) we have

$$\partial_{q,i} = [\delta_i^j + H_i^j] \partial_{x,j}, \quad \text{where} \quad H_{ij}(\mathbf{q}, \tau) \equiv \partial_{q,i} s_j(\mathbf{q}, \tau) \quad (2.4)$$

is the Lagrangian distortion tensor (frequently also denoted as $\Psi_{j,i}$). Second, by choosing the Lagrangian coordinates such that equal infinitesimal volume intervals $d^3\mathbf{q}$ contain equal amounts of matter, the matter density contrast δ is given by

$$1 + \delta(\mathbf{x}_\text{fl}(\mathbf{q}, \tau)) = \left| \frac{\partial \mathbf{x}}{\partial \mathbf{q}} \right|_{\mathbf{x}=\mathbf{x}_\text{fl}(\mathbf{q}, \tau)}^{-1} = |\mathbf{1} + \mathbf{H}(\mathbf{q}, \tau)|^{-1}, \quad (2.5)$$

where we denote 3-vectors and 3-tensors in boldface. Using Eq. (2.4) and Eq. (2.5), Eq. (2.2) can be transformed into an equation for \mathbf{H} which only refers to Lagrangian coordinates \mathbf{q} :

$$\text{tr} \left[(\mathbf{1} + \mathbf{H})^{-1} (\mathbf{H}'' + \mathcal{H}\mathbf{H}') \right] = -\frac{3}{2} \Omega_m \mathcal{H}^2 \left[|\mathbf{1} + \mathbf{H}|^{-1} - 1 \right]. \quad (2.6)$$

In the following, we will deal mostly with Lagrangian coordinates, and correspondingly drop the subscript q on derivatives; derivatives with respect to Eulerian coordinates x will be indicated explicitly.

LPT now works by treating the components of the distortion tensor as small parameters [21]; this is related to the expansion in powers of δ performed in Eulerian PT by Eq. (2.5). Specifically, we write

$$\mathbf{s}(\mathbf{q}, \tau) = \sum_{n=1}^{\infty} \mathbf{s}^{(n)}(\mathbf{q}, \tau), \quad (2.7)$$

and similarly for \mathbf{H} , where the solution for $\mathbf{s}^{(n)}$ involves n powers of the linear-order displacement $\mathbf{s}^{(1)}$. Eq. (2.6) can then be solved iteratively, where suitable manipulations show

that the source term only involves quadratic and cubic couplings. This in turn allows for convenient recursion relations [37–39].

First, we decompose the displacement (at any order) into longitudinal and transverse (or curl) components:

$$\mathbf{s} = \frac{\nabla}{\nabla^2} \sigma - \frac{1}{\nabla^2} \nabla \times \mathbf{t}, \quad (2.8)$$

where $\sigma \equiv \nabla \cdot \mathbf{s}$ denotes the divergence of the displacement, which only contributes to the symmetric part of \mathbf{H} , while the curl $\mathbf{t} = \nabla \times \mathbf{s}$ also sources the antisymmetric part of \mathbf{H} . Here, we have only allowed for solutions consistent with homogeneity, or equivalently periodic boundary conditions, allowing us to remove the constant solution and the solution $\propto \mathbf{x}$ in \mathbf{s} (see [40]). We will also assume that the spatial average of \mathbf{s} vanishes, likewise in keeping with periodic boundary conditions.

Second, we convert the time coordinate from conformal time τ to $\lambda \equiv \ln D$, the logarithm of the linear growth factor which is given by the growing solution to the linear ODE

$$D'' + \mathcal{H}D' - \frac{3}{2}\Omega_m \mathcal{H}^2 D = 0. \quad (2.9)$$

We now follow the treatment of Matsubara [39]. Combining Eqs. (26), (28), (31) and (59) there, we then obtain the following set of coupled ODE describing the evolution of the n -th order longitudinal and transverse contributions to \mathbf{H} :

$$\begin{aligned} \mathcal{D}_{3/2}(\lambda)\sigma^{(n)}(\mathbf{q}, \lambda) &= \sum_{m_1+m_2=n} \left\{ \text{tr} \left[\mathbf{H}^{(m_1)}(\mathbf{q}, \lambda) \mathcal{D}_{3/4}(\lambda) \mathbf{H}^{(m_2)}(\mathbf{q}, \lambda) \right] \right. \\ &\quad \left. - \text{tr} \left[\mathbf{H}^{(m_1)}(\mathbf{q}, \lambda) \right] \mathcal{D}_{3/4}(\lambda) \text{tr} \left[\mathbf{H}^{(m_2)}(\mathbf{q}, \lambda) \right] \right\} \\ &\quad - \frac{1}{2} \sum_{m_1+m_2+m_3=n} \varepsilon_{ijk} \varepsilon_{lmn} H_{il}^{(m_1)}(\mathbf{q}, \lambda) H_{jm}^{(m_2)}(\mathbf{q}, \lambda) \mathcal{D}_{1/2}(\lambda) H_{kn}^{(m_3)}(\mathbf{q}, \lambda) \\ \mathcal{D}_0(\lambda)(\mathbf{t}^{(n)})^i &= \sum_{m_1+m_2=n} \varepsilon^{ijk} \left(\mathbf{H}^{(m_1)} \mathcal{D}_0 \mathbf{H}^{(m_2)\top} \right)_{jk}, \end{aligned} \quad (2.10)$$

where

$$\begin{aligned} \gamma(\lambda) &\equiv \frac{\Omega_m(\lambda)}{f^2(\lambda)} - 1; \quad \lambda \equiv \ln D \\ \mathcal{D}_c &\equiv \frac{\partial^2}{\partial \lambda^2} + \frac{1}{2}[1 + 3\gamma(\lambda)] \frac{\partial}{\partial \lambda} - c[1 + \gamma(\lambda)] \quad \text{for any } c \in \mathbb{R}. \end{aligned} \quad (2.11)$$

Notice that contributions to the transverse source term with $m_1 = m_2$ vanish. For this reason, the transverse component begins at third order.

In a Euclidean matter-dominated (Einstein-de Sitter, EdS) universe, $\gamma = 0$, and the ODE can be solved analytically for the fastest growing mode. This leads to the simple recurrence relations given in Appendix A [30, 38]. In particular, both σ and \mathbf{t} factorize, i.e.

$$\sigma^{(n)}(\mathbf{q}, \lambda) = e^{n\lambda} \sigma^{(n)}(\mathbf{q}, \lambda = 0) \quad (2.12)$$

and similarly for the transverse component.

This factorization is essential both for an efficient evaluation of the LPT displacement, and for a closed bias expansion. Fortunately, the factorization is still possible even for a general expansion history [41]. For this, we write, at fixed order n in perturbations

$$\begin{aligned}\sigma^{(n)}(\mathbf{q}, \lambda) &= \sum_p [w_{n,p}^L e^{n\lambda} + \alpha_{n,p}^L(\lambda)] \sigma^{(n,p)}(\mathbf{q}, \lambda = 0) \\ \mathbf{t}^{(n)}(\mathbf{q}, \lambda) &= \sum_p [w_{n,p}^T e^{n\lambda} + \alpha_{n,p}^T(\lambda)] \mathbf{t}^{(n,p)}(\mathbf{q}, \lambda = 0),\end{aligned}\tag{2.13}$$

where p runs over the different shapes relevant at order n . Naively, one could expect one independent shape for each partition of n , however the actual number is significantly smaller due to the source term which only involves quadratic and cubic couplings, which are moreover symmetric in the m_i ; Tab. 1 schematically lists the different shapes relevant at the first few orders. The weights $w_{n,p}^{L,T}$ are set by the EdS solution (Appendix A), so that in EdS we simply have $\alpha_{n,p}^{L,T} = 0$, and all shapes at a given order have the same time dependence and can be combined into one linear combination.

In the code implementation, the contributions $\sigma^{(n,p)}$, $\alpha_{n,p}^L$ and $\mathbf{t}^{(n,p)}$, $\alpha_{n,p}^T$ are determined iteratively, starting from the linear order $n = 1$. At a given order n we determine the independent shapes generated by the source terms in Eq. (2.10), and integrate the ODE from deep in matter domination, starting with initial conditions $\alpha_{n,p}^{L,T} = 0 = \alpha_{n,p}^{L,T'}$. We only include independent shapes by restricting to $m_2 \geq m_1$ in the quadratic source term, and $m_3 \geq m_2 \geq m_1$ in the cubic source term. Note that each of these shapes in general corresponds to two or three different time dependencies in the source term coming from the permutations among the m_i , e.g. from $H^{m_1} \mathcal{D}H^{m_2}$ and $H^{m_2} \mathcal{D}H^{m_1}$ if $m_2 \neq m_1$. Since they multiply the same \mathbf{q} -dependent shape however, we combine them into a single $\alpha_{n,p}^{L,T}$.

This treatment is valid for any expansion history that has an extended period of matter domination; no assumption of an expansion history close to EdS is made at later times. The number of independent contributions to \mathbf{H} increases rapidly toward larger n ; for example, at $n = 5$ we have 9 independent longitudinal contributions (and 6 transverse ones), while these numbers grow to 23 (and 14) at $n = 6$. For the fiducial Λ CDM cosmology, $\alpha_{n,p}^{L,T}$ grows to at most ~ 0.002 at $z = 0$.

In the results for this paper, we also neglect the contribution of the transverse displacement \mathbf{t} to the source terms in Eq. (2.10). This is only formally accurate up to fourth order, since \mathbf{t} yields a trace-free contribution to the symmetric part of \mathbf{H} (see e.g. [25]). These contributions are derived in Appendix B. We have found that their impact on all statistics considered here is very small ($\lesssim 10^{-4} - 10^{-3}$ depending on the value of the cutoff), significantly smaller at low z than the effect of incorporating the exact Λ CDM expansion history. This is because the transverse part of the displacement is always much smaller than the longitudinal part (note that this is also a consequence of assuming only scalar initial perturbations, i.e. vanishing initial \mathbf{t}). On the other hand, the additional shapes generated by source terms involving \mathbf{t} substantially increase the memory requirement.

The construction of the Eulerian density field proceeds as follows:

1. $\sigma^{(1)} = -\delta^{(1)}$ is obtained from a given linear density field on a uniform cubic grid of size N_g^3 (the choice of grid size will be discussed below). In this paper, $\delta^{(1)}$ corresponds to the initial conditions used for the N-body simulations. A sharp- k filter on the scale $\Lambda_{\text{in}} = \Lambda$ is applied.
2. \mathbf{M} and \mathbf{t} are constructed on the same grid as described above.

3. \mathbf{s} is constructed by evaluating Eq. (2.8) on the grid. Note that $\mathbf{s}^{(n)}(\mathbf{k})$ has Fourier-space support up to $k = n\Lambda$.
4. $\mathbf{s}(\mathbf{k})$ is copied to a larger grid of size N_{CIC}^3 in Fourier space (“CIC grid”), and Fourier-transformed to real space.
5. The displacement is then evaluated at each position \mathbf{q} in the CIC grid, and mass $m_{\text{CIC}} = 1$ assigned to the Eulerian position $\mathbf{x} = \mathbf{q} + \mathbf{s}(\mathbf{q})$ using a cloud-in-cell (CIC) assignment scheme on the grid scale.

The use of pseudo-particles and density assignment in the last step ensures the conservation of mass at machine precision. This is important in order to avoid spurious noise on large scales, and would not be ensured if one were to expand Eq. (2.5) in the displacement directly. The approach described here is very similar to that taken in initial conditions generators for N-body simulations (e.g., [42, 43]). The main differences are that we go to higher orders in LPT, include beyond-EdS corrections, and apply a sharp- k cut on the linear density field before the LPT construction. Recently, Ref. [44] described a very similar scheme.

The final result is the Eulerian density field $\delta(\mathbf{x}, \tau)$ on a grid of size N_{CIC}^3 at a given time τ , to any desired order in LPT, and for any expansion history. We next turn to the construction of the fields appearing in the bias expansion of tracers.

3 Bias expansion at leading order in derivatives

The Lagrangian distortion tensor $\mathbf{H}(\mathbf{q}, \tau)$ captures all leading gravitational observables for an observer comoving with matter on the trajectory labeled by the Lagrangian coordinate \mathbf{q} , as shown in [30], where “leading” refers to leading order in spatial derivatives. This means that, as a function of Lagrangian coordinate and at leading order in derivatives, the galaxy density can be written as a nonlinear functional in time, F_g , of \mathbf{H} :

$$\delta_g(\mathbf{q}, \tau) = \int_0^\tau d\tau' F_g[\mathbf{H}(\mathbf{q}, \tau'); \tau'; \tau]. \quad (3.1)$$

In the perturbative regime, we then expand F_g in powers of \mathbf{H} , leading to the appearance of all rotational invariants of $\mathbf{H}(\mathbf{q}, \tau')$, such as $\text{tr}[\mathbf{H}]$, in general evaluated at different points in time. If every contribution to these invariants can be written in separable form, as in Eq. (2.13), then the integral over τ' in Eq. (3.1) can be formally done, leading to a bias expansion of the form

$$\delta_g(\mathbf{q}, \tau) = \sum_O b_O(\tau) O^L(\mathbf{q}, \tau), \quad (3.2)$$

n	Shapes contributing to $\mathbf{H}^{(n)}$ (schematic)
1	$H^{(1)}$
2	$H^{(1)}H^{(1)}$
3	$H^{(1)}H^{(2)}, H^{(1)}H^{(1)}H^{(1)}$
4	$H^{(1)}H^{(3,1)}, H^{(1)}H^{(3,2)}, H^{(2)}H^{(2)}, H^{(1)}H^{(1)}H^{(2)}$

Table 1. Different schematic shapes contributing to $\mathbf{H}^{(n)}$ at a given order n for general expansion histories.

where $b_O(\tau)$ absorbs the unknown small-scale physics encoded in F_g , and the sum runs over a specific set of Lagrangian bias operators O^L . Note that we have to allow for a different bias coefficient for each distinct time dependence appearing in the expansion of the invariants constructed out of \mathbf{H} (see [45] for the analogous treatment in the Eulerian case). While this bias construction was previously largely done under the simplifying EdS assumption, the approach continues to work for general expansion histories thanks to the separable LPT solution for \mathbf{H} in Eq. (2.13).

Let us now describe how to construct the set of complete bias operators O^L at leading order in derivatives. We begin by separating the distortion tensor \mathbf{H} into symmetric and antisymmetric parts:

$$H_{ij} = M_{ij} + C_{ij}, \quad \text{where} \quad M_{ij} = M_{ji}; \quad C_{ij} = -C_{ji}. \quad (3.3)$$

This is also convenient for the numerical implementation. The relation of \mathbf{M} and \mathbf{C} to the longitudinal and transverse parts of the displacement, σ and \mathbf{t} , is given in Eq. (B.2).

The set of Lagrangian bias operators O^L now comprises all scalar combinations (rotational invariants) of the contributions to the *symmetric part* of the Lagrangian distortion tensor, $\mathbf{M}^{(n,p)}$, with the following exception: $\sigma^{(n,p)} \equiv \text{tr}[\mathbf{M}^{(n,p)}]$ with $n > 1$ and any p does not have to be included, since it can be re-expressed in terms of lower-order terms using the LPT recursion relations. This implies that the bias expansion at order $n > 1$ only requires the $\mathbf{M}^{(m,p)}$ up to $m = n - 1$. The transverse displacement \mathbf{t} is likewise determined by the set of $\mathbf{M}^{(m,p)}$ at lower orders, and hence does not need to be included separately. For this reason, it is sufficient to include only the symmetric part \mathbf{M} in the bias expansion (whether or not the contribution from \mathbf{t} is included in \mathbf{M} is irrelevant for the completeness of the bias expansion, and only corresponds to a change of basis).

Previous references (e.g., [16]) have listed the complete set of bias operators (at leading order in derivatives and assuming the EdS approximation) up to fourth order. We now describe how the general set of operators is constructed up to any order. The building blocks are the set $\{\mathbf{M}^{(m,p)}\}_{m=1,\dots,n-1}^p$, where p again denotes the different shapes that exist at a given order m for a general expansion history; in case of the EdS approximation, there is only a single shape at each order. The enumeration of the n -th order bias expansion then proceeds as follows:

1. We first construct all scalar invariants up to including n -th order out of the $\mathbf{M}^{(m,p)}$. Given the restriction on $\text{tr}[\mathbf{M}^{(m,p)}]$, and since these are symmetric 3-tensors, the invariants at order m consist of the set

$$\begin{aligned} \mathcal{I}^{(m)} &= \left\{ \text{tr}[\mathbf{M}^{(1)}], \quad \left\{ \text{tr}[\mathbf{M}^{(m_1,p_1)} \mathbf{M}^{(m_2,p_2)}] \right\}_{m_1+m_2 \leq m}^{p_1,p_2}, \right. \\ &\quad \left. \left\{ \text{tr}[\mathbf{M}^{(m_1,p_1)} \mathbf{M}^{(m_2,p_2)} \mathbf{M}^{(m_3,p_3)}] \right\}_{m_1+m_2+m_3 \leq m}^{p_1,p_2,p_3} \right\} \\ &\equiv \left\{ I_s^{(m)} \right\}_{s=1}^{N_{\mathcal{I}}(m)}. \end{aligned} \quad (3.4)$$

2. We then construct all independent products

$$\begin{aligned} I_{s_1}^{(m_1)} \dots I_{s_k}^{(m_k)}, \quad 1 \leq k \leq n, \\ \text{with} \quad m_1 + \dots + m_k = n; \quad s_i \in \{1, \dots, N_{\mathcal{I}}(m_i)\}. \end{aligned} \quad (3.5)$$

Technically, this is done iteratively by running over the set of partitions of n , and then, for each partition $\{m_i\}_{i=1}^k$, constructing products of all combinations of the $\{s_1, \dots, s_k\}$.

This construction works up to any order n , although the number of independent operators increases rapidly toward larger n . As already shown in App. C of [16], the first bias term that is *not* present in the EdS approximation appears at fourth order, where $\text{tr}[\mathbf{M}^{(3)}\mathbf{M}^{(1)}]$ generalizes to

$$\text{tr}[\mathbf{M}^{(3,1)}\mathbf{M}^{(1)}], \quad \text{tr}[\mathbf{M}^{(3,2)}\mathbf{M}^{(1)}]. \quad (3.6)$$

The number of additional bias operators that appear when going beyond the EdS approximation likewise increases rapidly at orders $n > 4$, as can be inferred from Tab. 1.

After the construction of the set of Lagrangian bias operators, each operator is displaced to Eulerian space using the displacement field $\mathbf{s}(\mathbf{q})$ following the description at the end of Sec. 2, where the mass m_{CIC} of each pseudo-particle is now given by the respective operator:

$$m_{\text{CIC}}^O(\mathbf{q}) = O^L(\mathbf{q}). \quad (3.7)$$

This follows the same treatment as in [17], where the Zel'dovich displacement was used for \mathbf{s} . Note that, due to the Jacobian of the displacement to Eulerian space, the displacement transforms each operator according to

$$O^L(\mathbf{q}) \rightarrow O(\mathbf{x}) = [1 + \delta(\mathbf{x})]O^L(\mathbf{q}[\mathbf{x}]). \quad (3.8)$$

At leading order in perturbations, this corresponds to the desired result, $O^L(\mathbf{q}[\mathbf{x}])$. At higher orders, since the bias expansion contains all combinations of operators, the prefactor $1 + \delta$ can be absorbed by a redefinition of bias parameters.

4 Higher-derivative bias

Having described the construction of the complete bias expansion at any order in *perturbations*, we next turn to the expansion in *derivatives*. In general, this expansion is controlled by the parameter $(kR_*)^2$, where k is the wavenumber and R_* is a spatial length scale that is specific to a given tracer. For halos, this scale is expected and found to be of order the Lagrangian radius [5, 46, 47], but for real galaxies it could be substantially larger (e.g., [48–50]), so that the ability to include higher-derivative bias operators is potentially important. Even for halos, Ref. [1] found them to be numerically relevant at sufficiently high order in perturbations.

At k -th order in derivatives, the fundamental ingredients of the bias expansion are all invariants constructed from $\nabla \cdots \nabla \mathbf{M}^{(m,p)}$, with up to k derivatives acting on any $\mathbf{M}^{(m,p)}$ (see Sec. 2.6 of [16]). Notice that k has to be even, since all indices need to be contracted (there are no preferred directions); the number of derivatives acting on a single instance of $\mathbf{M}^{(m,p)}$ can be odd of course.

The full set of higher-derivative terms is unfortunately cumbersome for several reasons. First, the memory requirements for constructing the tensor $\nabla \cdots \nabla \mathbf{M}^{(m,p)}$ increase exponentially with the number of derivatives. Second, there are degeneracies between higher-derivative terms which are not trivial to remove. As a simple example, consider only terms involving $\sigma^{(1)} = \text{tr}[\mathbf{M}^{(1)}]$. We have, for $k = 2$ and $n = 2$,

$$\nabla^2(\sigma^{(1)})^2, \quad (\nabla\sigma^{(1)})^2, \quad \sigma^{(1)}\nabla^2\sigma^{(1)}, \quad (4.1)$$

only two of which are independent. In this case, the degeneracy is obvious, but it is much more difficult to identify and remove at higher orders.

Since an exact degeneracy between different bias terms can lead to severe numerical issues when sampling parameters or attempting to find the maximum of the likelihood, we instead opt for the following simplification. Let \mathcal{O} be the set of Eulerian bias operators constructed up to some order n in perturbations and k in derivatives, and $n(O)$ be the order in perturbations of a given operator O . The set at order n in perturbations and $k + 2$ in derivatives is then constructed by adding the set

$$\{\nabla^2 O\}_{O \in \mathcal{O}} \cup \{\nabla O' \cdot \nabla O\}_{O, O' \in \mathcal{O}: n(O) + n(O') \leq n} \cup \{O' \nabla^2 O\}_{O, O' \in \mathcal{O}: O \neq O' \wedge n(O) + n(O') \leq n} \quad (4.2)$$

to the set of operators, where for the terms involving two operators O, O' only one permutation of each pair is included. This construction is used to iteratively add derivatives starting from $k = 0$ to the desired order.

While this approach only includes a subset of all *nonlinear* higher-derivative bias operators, these are guaranteed to be linearly independent, and no significant additional memory is needed (apart from that needed to store the operators themselves). The leading higher-derivative terms that are not included are

$$\partial_k M_{ij}^{(1)} \partial^k M^{(1)ij} \quad (4.3)$$

and other contractions of the same type, while all higher-derivative terms involving $\text{tr}[\mathbf{M}^{(1)}]$ are included.

In practice, since the displacement from Lagrangian to Eulerian space is the costliest step in the forward model, we generate the higher-derivative operators in Eulerian space, i.e. apply $\nabla = \nabla_x$ after the displacement operation Eq. (3.8). For a complete set of higher-derivative operators, the choice of Eulerian or Lagrangian derivatives is irrelevant, as the differences between ∇_q and ∇_x can be absorbed by shifting bias parameters, via Eq. (2.4) (see Sec. 2.6 of [16]). For the reasons explained above, the set of higher-derivative operators implemented here is not complete, so the corresponding Lagrangian and Eulerian subsets are not equivalent. We leave a detailed investigation of the practical relevance of the missing higher-derivative operators, and the choice of Eulerian vs Lagrangian derivatives to future work.

5 Numerical implementation

The forward model described above is implemented in an OpenMP-parallelized C++ code centered around classes encapsulating scalar, vector, and tensor grids. Fast Fourier transforms of the grids are done using FFTW3. Multiplications are performed in real space, while derivatives (including negative powers) are performed in Fourier space. The grid resolution is always chosen to capture all relevant modes, so that no kernel deconvolutions are necessary. These aspects are very similar to the implementation described in [44], which however is distributed-memory capable.

Several density assignment schemes are available, including nearest grid point and Fourier-Taylor up to next-to-leading order (see [34]). However, all results shown here use the standard cloud-in-cell density assignment on the given grid scale; specifically, we choose $N_{\text{CIC}} = 512$ for the Eulerian assignment grid in the forward model (see Sec. 2), as well as the simulation output (dark matter particles and halos). The Nyquist frequency of the Eulerian grid for the simulation box used here, $L_{\text{box}} = 2000 h^{-1} \text{Mpc}$ is $k_{\text{Ny}}^{\text{CIC}} \simeq 0.8 h \text{Mpc}^{-1}$, far beyond the maximum wavenumbers explored here. Moreover, by using the same assignment scheme

in the forward model as well as for simulated tracers, the assignment kernel cancels in the comparison.

The code additionally contains functionality to copy grids to higher and lower resolutions, matching all Fourier modes up to the smallest Nyquist frequency involved. We refer to [1] for the details of the Nyquist plane treatment. A public release of the code is planned for the future.

Finally let us turn to the choice of grid resolution for the forward model. Throughout, we consider an n -th order forward model constructed from the linear density field with a sharp- k filter with cutoff Λ . The results of this forward model are then only used in comparison to “observations” on scales $k < \Lambda$. Then, there are two possible choices:

1. *No mode left behind:* in order to ensure that *all* couplings of the linear modes up to $k = \Lambda$ are captured, one has to choose $k_{\text{Ny}} = n\Lambda$, which implies

$$N_g(\Lambda) = \left\lceil n \frac{L_{\text{box}}\Lambda}{\pi} \right\rceil. \quad (5.1)$$

2. *Generalized Orszag rule:* if the only concern is to avoid aliasing of high- k modes to low k , it is sufficient to require

$$N_g(\Lambda) = \left\lceil \frac{n+1}{2} \frac{L_{\text{box}}\Lambda}{\pi} \right\rceil. \quad (5.2)$$

This is because the lowest aliased modes have wavenumbers $k_{\text{alias}} = 2k_{\text{Ny}} - n\Lambda$, which has to be greater than Λ to avoid aliased modes on the range of wavenumbers used (see also [4]; the special case of $n = 2$ is also known as Orszag’s rule [51]).

The memory requirements of the first option are significantly higher. If the mode coupling of high- k modes far above the cutoff Λ has a subdominant effect on the low- k modes used in the comparison with data, then the second option is a good approximation. In fact, in the effective field theory (EFT) approach the effect of this type of mode coupling is absorbed by the counterterms; hence, the generalized Orszag rule might be sufficient if counterterms are allowed for. We will present some results in this scheme below, since it allows for higher cutoff values to be probed, but leave a more detailed exploration (including the possibility of further reducing N_g) for future work.

The reasoning above does not apply to the Eulerian grid of size N_{CIC}^3 used for the density assignment. This is a fully nonlinear (in terms of the relation between displacement and resulting field), but local operation. No aliasing is induced for low- k modes, since the procedure preserves mass to machine precision. Moreover, the same assignment procedure is applied to the data (N-body particles in case of the results here; halos in case of [1]).

The simulation results used here are the same as those used in [1, 13, 34], performed using the GADGET-2 code [52]. Specifically, we use simulations started with particles displaced using 2LPT at the starting redshift $z_{\text{in}} = 24$, as these have substantially reduced transients (see [1] for a discussion). We also make use of simulations initialized in the same way, but using a linear density field with a sharp- k cutoff at $\Lambda_{\text{in}} = 0.1 h \text{ Mpc}^{-1}$ and $\Lambda_{\text{in}} = 0.2 h \text{ Mpc}^{-1}$.

6 Comparison with N-body simulations

We now turn to the comparison of the forward model described here with full N-body simulations. We focus here on the matter density field itself. Results for dark matter halos,

specifically cosmology inference using the EFT likelihood, were already shown in [1]. We leave further studies on halos and other tracers, such as comparisons of n -point correlation functions, to future work.

In particular, we will consider three comparisons here: (1) *Matter power spectrum in simulations with cutoff*: in this case, the N-body code essentially solves LPT to arbitrarily high order, so that this comparison serves to test the LPT implementation as well as the asymptotic series of the LPT expansion (see also [53]). (2) *Matter power spectrum and correlation coefficient in simulations without cutoff*: the comparison with full, non-perturbative simulations allows for the estimation of the size and scale dependence of the EFT counterterms for matter, in particular the effective sound speed. (3) *σ_8 profile likelihood*: as a test for the quality of the LPT prediction for higher-order statistics, we study the σ_8 inference from dark matter particles allowing for the linear bias b_1 to be free, which removes the linear-order information on σ_8 in the matter density field (corresponding essentially to the power spectrum).

6.1 Simulations with cutoff

Fig. 1 shows the fractional deviation (in percent) between the power spectrum in the LPT forward model and that in N-body simulations that use the same cutoff in the initial conditions. This very large-scale cutoff, by simulation standards, essentially makes the result of the N-body code an arbitrary-order LPT solution, so that the asymptotic properties of the LPT series expansion can be tested. It is worth emphasizing that most of the cases shown in Fig. 1 are likely beyond the strict convergence radius of LPT; see [44] for a recent numerical determination of this scale using a Λ CDM linear power spectrum, and [38, 54] for more theoretical considerations. Thus, one expects the deviation of successively higher LPT orders to shrink initially, and then increase again as higher-order terms are no longer suppressed.

Even keeping this in mind, one should note that for $n > 2$, n -th order LPT agrees with the N-body result to better than $\sim 0.1\%$ for $k \lesssim \Lambda$ in the case of $\Lambda = 0.1 h \text{Mpc}^{-1}$. This excellent agreement is made possible by using precisely the same density assignment scheme for both LPT as well as N-body “particles,” and by using the “no mode left behind” requirement for the grid size. The agreement with simulations is noticeably worse if the generalized Orszag rule is used instead, showing that, when comparing to simulations with a cutoff, the coupling of modes significantly above the cutoff to lower- k modes is not negligible.

At $\Lambda = 0.1 h \text{Mpc}^{-1}$ and $z = 0$, one can conclude that the LPT expansion improves at least to order $n = 6$. Note however that the improvement when going from $n = 3, 4$ to $n = 5, 6$ is less clear at higher z . Turning to the higher cutoff value of $\Lambda = 0.2 h \text{Mpc}^{-1}$, we see qualitatively similar results to the lower cutoff case, but with stronger deviations from the N-body result, as expected. In this case, the large memory requirements (a factor of 8 times larger than for $\Lambda = 0.1 h \text{Mpc}^{-1}$ at the same order) restrict us to fifth order. Even at $z = 0$, 5LPT still significantly improves upon 4LPT.

The main caveat in this comparison is that the N-body simulations necessarily have transients from the initial conditions, which become more important at higher redshifts. The points in Fig. 1 show the deviation in the matter power spectrum in simulations started from 2LPT initial conditions at $z_{\text{in}} = 99$ instead of the default $z_{\text{in}} = 24$, with identical parameters otherwise. For $\Lambda = 0.1 h \text{Mpc}^{-1}$, these deviations, which are thus due to transients from the initial conditions, are of the same order as the difference between the simulations and high-order LPT. This also holds for $\Lambda = 0.2 h \text{Mpc}^{-1}$ at $z = 1$. Hence, firm conclusions on the asymptotic properties and accuracy of LPT in these cases can only be reached once

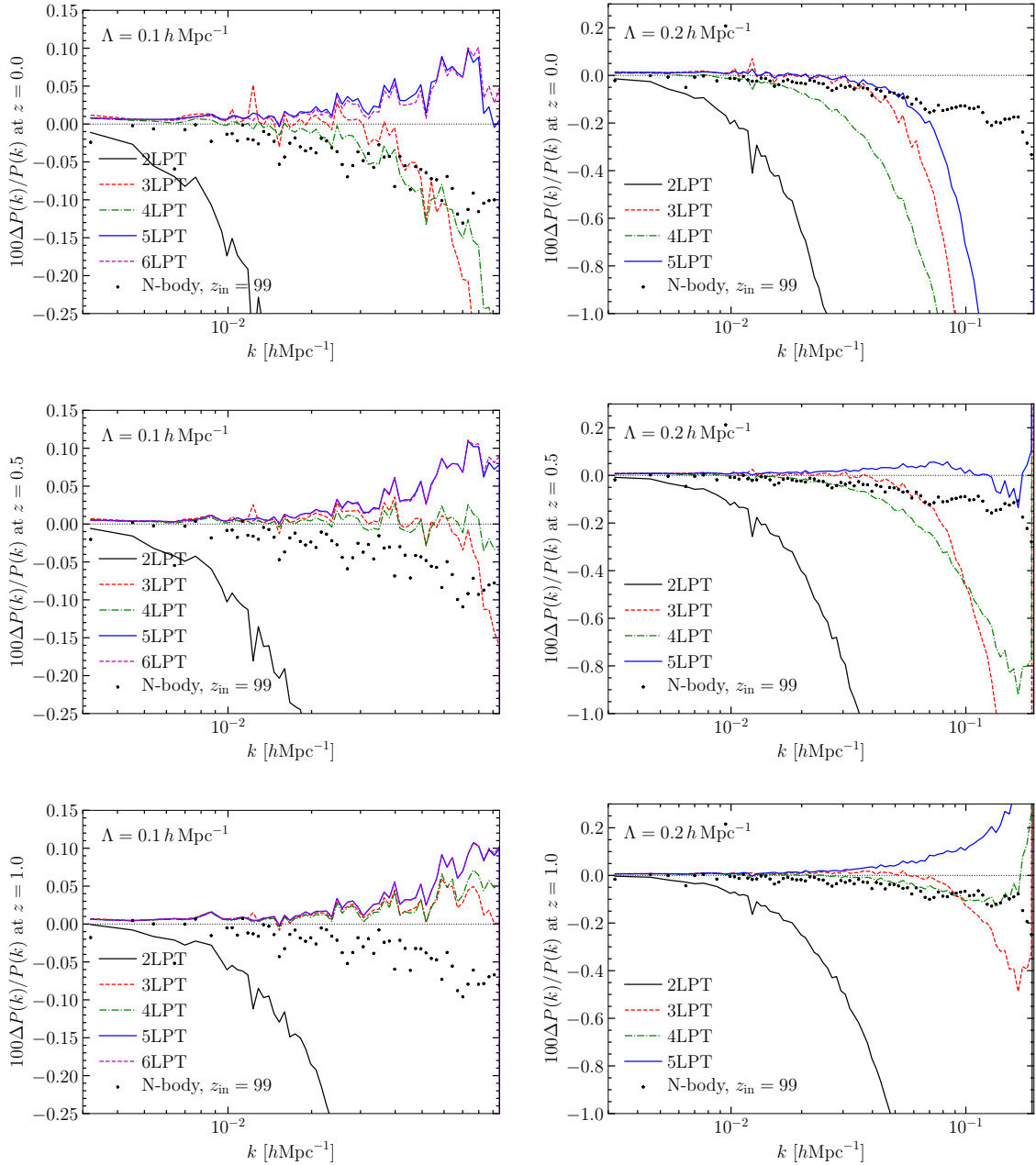


Figure 1. Relative deviation (in percent) of the matter power spectrum measured in the LPT forward model output at different orders from that measured in N-body simulations, both using the same initial cutoff Λ , Eulerian density grid, and assignment kernel. The left panels show results for $\Lambda = 0.1 h \text{ Mpc}^{-1}$, while the right panels show the same for $\Lambda = 0.2 h \text{ Mpc}^{-1}$, each at redshifts $z = 0, 0.5, 1$ (top, middle, and bottom panels, respectively). The exact time dependence for each shape is used in the LPT forward model. The dotted points show the corresponding deviation of the matter power spectrum in an N-body simulation started at $z_{\text{in}} = 99$ instead of $z_{\text{in}} = 24$, illustrating the order of magnitude of transients from the initial conditions.

transients have been rigorously quantified. We will defer this study to future work; see e.g. [55–57] for in-depth discussions of transients.

The results shown so far use the general time dependence of each shape by numerically integrating the corresponding equations in $\lambda = \ln D$ for the Λ CDM expansion history. However, the change from the EdS approximation is minor, as shown in Fig. 2 for $z = 0$, where the effects of the different expansion histories is largest. The predictions for the exact expansion history are larger than the EdS approximation by 0.1 – 0.2%, depending on the cutoff value. This does generally improve the agreement with the N-body result noticeably. While a correction of order 0.1 – 0.2% might be negligible in many applications, it is worth noting that the magnitude of this correction will depend on cosmology. In particular, a cosmological model that differs from EdS more substantially than Λ CDM, especially at higher redshifts, might lead to bigger effects. Unfortunately, due to the greatly increased number of shapes (grids) that need to be independently computed, the memory requirements for the general expansion history case are significantly larger than for EdS.

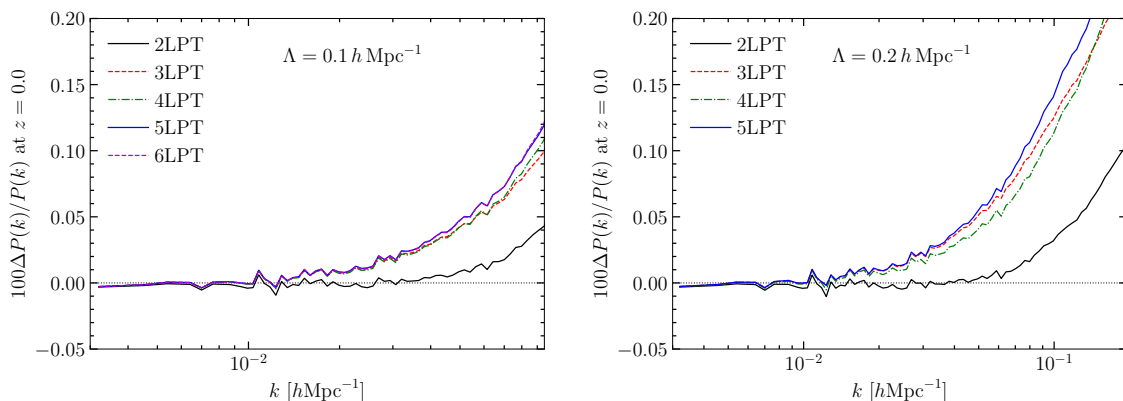


Figure 2. Ratio of LPT power spectra for the general expansion history and using the EdS approximation, both with initial cutoff at $\Lambda_{\text{in}} = 0.1 h \text{ Mpc}^{-1}$ (left panels) and $\Lambda_{\text{in}} = 0.2 h \text{ Mpc}^{-1}$ (right panels) at $z = 0$. In case of Λ CDM, the prediction using the exact expansion history is always slightly larger than the result using the EdS approximation.

6.2 Full simulations

We now turn to the comparison with full N-body simulations. In this case, we expect a residual contribution to the density field from the small-scale, fully nonlinear modes even for $k < \Lambda$, which at leading order takes the form of an effective sound speed [58, 59]:

$$\delta_{\text{c.t.}}^{(1)}(\mathbf{k}, \tau) = -C_{s,\text{eff}}^2(\Lambda, \tau) k^2 \delta(\mathbf{k}, \tau). \quad (6.1)$$

Note that for the present application, $C_{s,\text{eff}}^2$ also depends on the cutoff Λ , although we will not write this dependence explicitly in what follows for the sake of clarity. The effective sound speed is only the leading EFT counterterm to the matter density field; one also expects quadratic contributions as well as a stochastic contribution to the power spectrum that scales as k^4 . Here, however, we will restrict to the investigation of the leading counterterm; see [4] for a detailed study of counterterms in the LPT context.

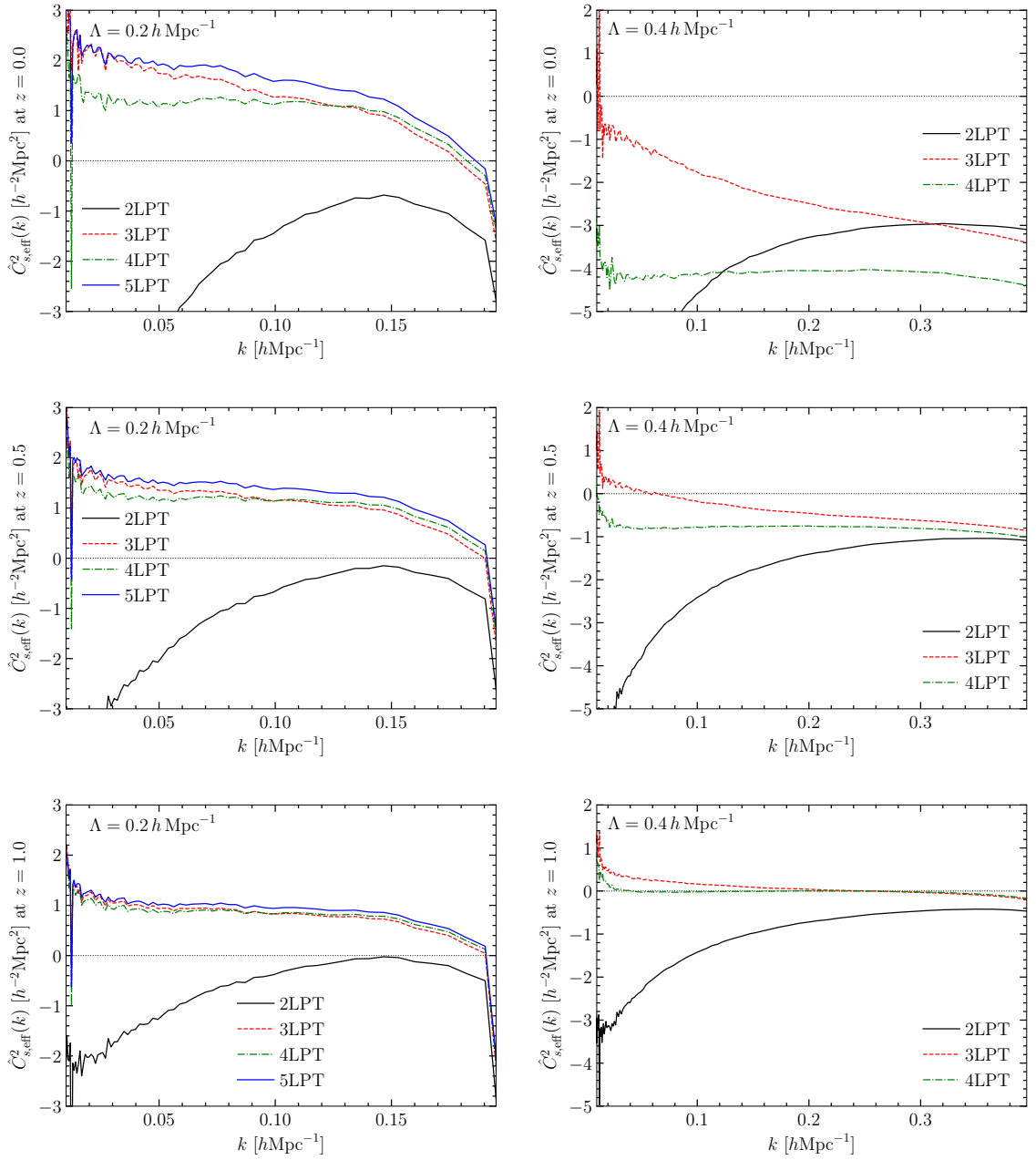


Figure 3. Effective sound speed of matter $\hat{C}_{s,\text{eff}}^2(k)$ for full N-body simulations, estimated through Eq. (6.3) for different LPT orders and cutoff values of $\Lambda = 0.2 h \text{Mpc}^{-1}$ (left panels) and $\Lambda = 0.4 h \text{Mpc}^{-1}$ (right panels), at different redshifts $z = 0, 0.5, 1$ (top, middle, and bottom panels, respectively). The exact time dependence is used in the LPT construction. For the cutoff value of $\Lambda = 0.4 h \text{Mpc}^{-1}$, we use the generalized Orszag rule for determining the minimum k_{Ny} at each order.

The counterterm in Eq. (6.1) contributes to any perturbative prediction for the matter power spectrum through

$$P_{m,\text{EFT}}(k, \tau) = \left[1 - 2C_{s,\text{eff}}^2(\tau)k^2\right] P_{m,\text{LPT}}(k, \tau) + \text{higher order}, \quad (6.2)$$

where we have defined $C_{s,\text{eff}}^2$ to multiply the full PT-predicted density field. Setting the left-hand side equal to the N-body power spectrum, we can solve for $C_{s,\text{eff}}^2$ as a function of scale and time,

$$\hat{C}_{s,\text{eff}}^2(k, \tau) = -\frac{P_{m,\text{N-body}}(k, \tau) - P_{m,\text{LPT}}(k, \tau)}{2k^2 P_{m,\text{LPT}}(k, \tau)}, \quad (6.3)$$

in our case for different LPT orders, $P_{m,\text{LPT}}$, and for different cutoff values. At leading order, we then expect a scale-independent result for $\hat{C}_{s,\text{eff}}^2$, while any nontrivial k -dependence indicates the presence of higher-order perturbative or counterterm corrections.

The result is shown in Fig. 3. The left panels show a cutoff value which we have seen is still under perturbative control, i.e. all modes entering the forward model are still in the quasilinear regime. The trends seen qualitatively reflect those of Fig. 1: for 2LPT, $\hat{C}_{s,\text{eff}}^2$ shows a strong scale dependence, while the scale dependence becomes much weaker at higher orders. 4LPT shows the weakest scale dependence in this case. Note that as k approaches Λ , the scale dependence of $\hat{C}_{s,\text{eff}}^2$ becomes stronger. This is expected, since $\hat{C}_{s,\text{eff}}^2$ has to capture the effect of all modes above Λ . For k approaching Λ , the coupling with modes above the cutoff can no longer be captured by the simple counterterm in Eq. (6.1); equivalently, one can think of Eq. (6.1) as being an expansion in k^2/Λ^2 , with only the leading term being included.

Perturbation-theory predictions of the matter power spectrum and other statistics typically do not employ an explicit cutoff as done in this forward model (but see [34, 35, 60]). Instead, the cutoff is sent to infinity, or at least large values, so that loop integrals run over arbitrarily large momenta. In order to get closer to this case, we show results for $\Lambda = 0.4 h \text{Mpc}^{-1}$ in the right panels of Fig. 3. In this case, we use the generalized Orszag rule to determine the grid size, substantially reducing the memory requirements. This can be justified by the fact that the coupling of several high- k modes to a low k -mode that is being “left behind,” i.e. not captured on the grid, should be absorbed by the counterterm. Interestingly, we indeed find that the scale dependence of $\hat{C}_{s,\text{eff}}^2$ is moderate for 3LPT, and in fact very small for 4LPT. This indicates that 4LPT with a high cutoff, combined with a single scale-independent $C_{s,\text{eff}}^2(\tau)$, can describe the matter power spectrum to the few-percent level at least up to $k \lesssim 0.4 h \text{Mpc}^{-1}$. Care should be taken however, as this amounts to extrapolating the perturbative prediction past its regime of validity.

Several measurements of the effective sound speed have been presented in the literature [4, 47, 61–63], most of which have been based on Eulerian perturbation theory. The closest comparison point is offered by [4]. Fig. 9 there shows results for 3LPT and $\Lambda = 0.61 h^{-1} \text{Mpc}$, measured using different approaches. The value of $\hat{C}_{s,\text{eff}}^2$ (corresponding to α there) is in broad agreement at $k \simeq 0.1 h \text{Mpc}^{-1}$ for both $z = 0$ and $z = 0.5$. However, the scale dependence shows some differences, which is likely attributable to the different cutoff Λ , as well as different estimators used.

One particular aspect of the results in Fig. 3 is noteworthy: while $\hat{C}_{s,\text{eff}}^2$ is in general scale-dependent, this scale dependence is smooth and does not show any signatures of the BAO. This means that BAO damping is captured very accurately by the LPT forward model, which is in contrast to Eulerian PT approaches (see Fig. 6 of [63] for a clear illustration).

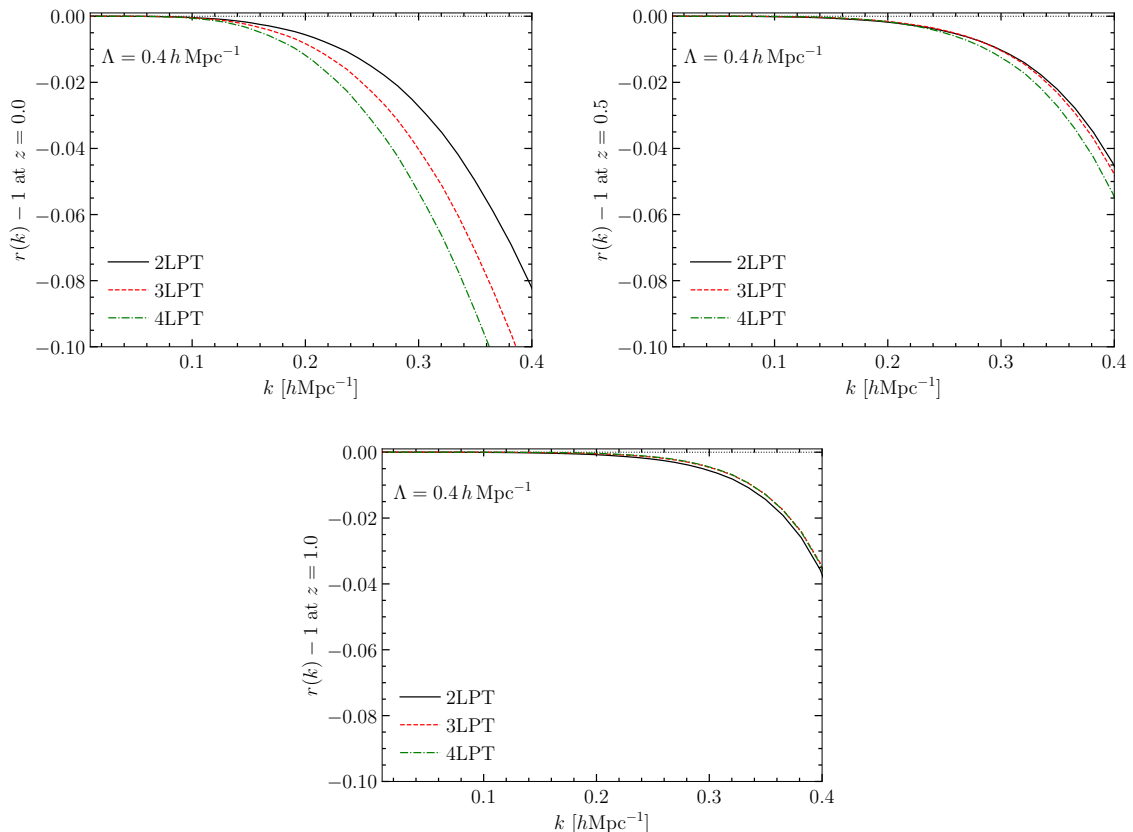


Figure 4. Correlation coefficient between the n -LPT density field with exact time dependence and the full N-body density field, for $\Lambda = 0.4 h \text{Mpc}^{-1}$ at different redshifts. Here, we have used the generalized Orszag rule for determining the minimum k_{Ny} .

Finally, Fig. 4 shows the correlation coefficient (more precisely, its deviation from unity) between the n -LPT density field and the full N-body density field. The correlation is clearly very high even for nonlinear scales, confirming previous results (going back to [53, 64, 65]). Interestingly, at $z = 0$, the best correlation coefficient is obtained by 2LPT, although the difference between the different LPT orders is rather small. It is also worth noting that the LPT density using the EdS approximation performs slightly worse (not shown here). At $z > 0.5$, all LPT orders essentially yield the same correlation coefficient. The fact that higher LPT orders lead to a worsening correlation coefficient for $\Lambda = 0.4 h \text{Mpc}^{-1}$ at $z = 0$ is likely attributable to the fact that one is going significantly beyond the convergence radius of LPT for such a high cutoff value. The comparison with $\Lambda = 0.2 h \text{Mpc}^{-1}$ at $z = 0$, which does not exhibit this behavior, confirms this (not shown here).

6.3 Profile likelihood for σ_8

The profile likelihood as a tool to study cosmology inference from nonlinear structure in the simulation setting, i.e. when the initial conditions are known, has been studied extensively recently [1, 13, 34]. Those studies focused on the inference of σ_8 from halo catalogs in real space. Due to the perfect degeneracy between the linear bias b_1 and σ_8 at linear order, this inference is based entirely on nonlinear information.

Here, we perform an analogous study using the dark matter density field from full N-body simulations as tracer field. In the inference, we leave b_1 and the higher-derivative bias $b_{\nabla^2\delta}$ free, while fixing all other bias parameters to zero. b_1 is left free to ensure that we test the nonlinear part of the density field, since the agreement of LPT and N-body density fields on large, linear scales was already established using the power spectrum above. The bias term $b_{\nabla^2\delta}$ essentially corresponds to the effective sound speed Eq. (6.1), and so should be allowed to vary in any case.

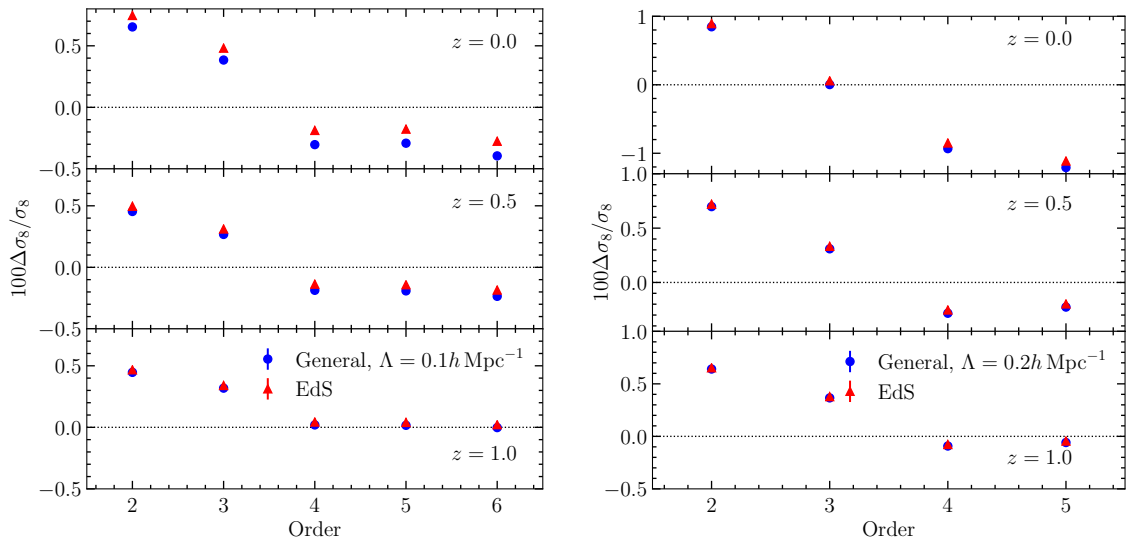


Figure 5. Fractional deviation from the ground truth (in percent) of the maximum-a-posteriori value for σ_8 inferred from the profile likelihood applied to the N-body matter density field. Results are shown for fixed cutoffs $\Lambda = 0.1 h \text{ Mpc}^{-1}$ (left panels) and $\Lambda = 0.2 h \text{ Mpc}^{-1}$ (right panels) as function of LPT order, at different redshifts $z = 0, 0.5, 1$ (top, middle, and bottom panels, respectively). In case of $\Lambda = 0.2 h \text{ Mpc}^{-1}$, the statistical error bars are too small to be seen here. Here, the linear bias b_1 and higher-derivative bias $b_{\nabla^2\delta}$ were left free, so that σ_8 inference is based on nonlinear information, while all other bias parameters are fixed to zero. We show results using the exact time dependence as well as the EdS approximation.

We then proceed exactly as described in [34] to infer σ_8 . The result, precisely the fractional deviation in percent of the inferred value of σ_8 from the ground truth, is shown in Fig. 5 as function of LPT order. We generally see improved agreement with increasing order in LPT, as expected in the converging regime of the asymptotic LPT expansion, with the exception of $\Lambda = 0.2 h \text{ Mpc}^{-1}$ at $z = 0$. For $z \geq 0.5$, LPT at fifth and higher order recovers the correct σ_8 to within 0.2% for both cutoff values, where one should recall that this inference is based on information *beyond the power spectrum* (and for fixed phases). This accuracy is very likely to be sufficient for any application to current and next-generation surveys. We again find that using the exact time dependence for ΛCDM only shifts the inferred σ_8 by at most $\sim 0.1\%$ relative to the EdS approximation.

7 Conclusions

We have presented an arbitrary-order Lagrangian forward model for the matter density field as well as that of biased tracers of large-scale structure. It includes the complete bias expan-

sion at any order in perturbations, and captures general expansion histories without relying on the EdS approximation (although the latter is also implemented and results in substantially smaller computational demands). A subset of the nonlinear higher-derivative terms in the bias expansion of general tracers is included as well.

We have studied the accuracy of this forward model, and the convergence properties of the asymptotic LPT expansion, focusing on the matter density field here. Results for biased tracers (halos) have already been presented in [1]. The findings can be summarized as follows:

- Comparing the matter power spectrum with N-body simulations using a cutoff $\Lambda = 0.1 h \text{ Mpc}^{-1}$ in the initial conditions, we find agreement to better than 0.1%.
- When comparing to full N-body simulations without cutoff, we were able to measure the effective sound speed. For relatively high cutoff values, corresponding to the case commonly employed in perturbative calculations, the effective sound speed is very close to scale-independent all the way up to $k \sim 0.4 h \text{ Mpc}^{-1}$, with no signs of oscillations, showing that BAO damping is captured very accurately.
- As a measure of the accuracy of the predicted density field beyond the power spectrum, we studied the inference of the primordial power spectrum normalization σ_8 , allowing for a free linear bias coefficient in order to remove the information from linear perturbations. In the regime where results converge as function of LPT order, we find agreement to 0.2% or better.

It would be interesting to test the convergence of LPT more systematically in the future, along the lines of [44]. Simulations with cutoff can serve as a new tool in this approach. Further, it is important to test the relevance of the neglected higher-derivative terms for biased tracers such as halos. Also, the forward model presented here is uniquely suited to exploring expansion histories beyond Λ CDM (e.g. with oscillating equation of state [66]).

Finally, in order to ready the forward model for the application to real data, redshift-space distortions and light-cone effects need to be included. Both of these can be straightforwardly incorporated in this approach; in case of the former, this was explicitly shown by [31], the latter are described in [14, 67]. We leave the implementation of these effects for future work.

Acknowledgments

I am indebted to Martin Reinecke for help in optimizing the code, and to Cornelius Rampf for pointing out the transverse contribution to \mathbf{M} . I further thank Tobias Baldauf, Giovanni Cabass, Oliver Hahn, Donghui Jeong, Guilhem Lavaux, Cornelius Rampf, Marcel Schmittfull, and Volker Springel for helpful discussions. Finally, I am grateful to Adrian Hamers for access to his large shared-memory computer cluster at MPA, which enabled results at higher orders in LPT. I acknowledge support from the Starting Grant (ERC-2015-STG 678652) ‘‘GrInflaGal’’ of the European Research Council.

A Einstein-de Sitter solution of LPT

In an Einstein-de Sitter universe, where $\Omega_m(a) = 1$ and the linear growth factor is $D(a) = a$ so that $\gamma \equiv 0$, all shapes of \mathbf{M} at a given order in perturbation theory have the same time

dependence $D^n(a)$. Then, the equation of motion Eq. (2.10) can be solved analytically to yield [30, 38]

$$\sigma^{(n)}(\mathbf{q}, y) = \sum_{m_1+m_2=n} c_{n,m_1,m_2}^{(\sigma)} \left\{ \text{tr} \left[\mathbf{M}^{(m_1)}(\mathbf{q}, y) \mathbf{M}^{(m_2)}(\mathbf{q}, y) \right] - \text{tr} \left[\mathbf{M}^{(m_1)}(\mathbf{q}, y) \right] \text{tr} \left[\mathbf{M}^{(m_2)}(\mathbf{q}, y) \right] \right\} - \frac{1}{2} \sum_{m_1+m_2+m_3=n} c_{n,m_1,m_2,m_3}^{(\sigma)} \varepsilon_{ijk} \varepsilon_{lmn} M_{il}^{(m_1)}(\mathbf{q}, y) M_{jm}^{(m_2)}(\mathbf{q}, y) M_{kn}^{(m_3)}(\mathbf{q}, y) \quad (\text{A.1})$$

$$(\mathbf{t}^{(n)})^i = \sum_{m_1+m_2=n} c_{n,m_1,m_2}^{(t)} \varepsilon^{ijk} \left(\mathbf{M}^{(m_1)} \mathbf{M}^{(m_2)\top} \right)_{jk}, \quad (\text{A.2})$$

where the weights are given by

$$c_{n,m_1,m_2}^{(\sigma)} = \frac{1}{2} \frac{m_1^2 + m_2^2 + (n-3)/2}{n^2 + (n-3)/2}; \quad c_{n,m_1,m_2,m_3}^{(\sigma)} = \frac{1}{3} \frac{m_1^2 + m_2^2 + m_3^2 + (n-3)/2}{n^2 + (n-3)/2};$$

$$c_{n,m_1,m_2}^{(t)} = \frac{1}{2} \frac{m_2 - m_1}{n}. \quad (\text{A.3})$$

This solution is used as initial condition at $\lambda = \ln(0.1)$ for the integration of Eq. (2.10) for a general expansion history. Results when using this solution at all times are also shown in the main text.

B Transverse contributions to LPT source terms

Let us write the Lagrangian distortion tensor at any given order as

$$H_{ij} = M_{ij} + C_{ij}, \quad (\text{B.1})$$

where

$$M_{ij} = M_{ji} = \frac{\partial_i \partial_j}{\nabla^2} \sigma - \varepsilon^{ikl} \frac{\partial_j \partial_k}{\nabla^2} t_l$$

$$C_{ij} = -C_{ji} = \frac{1}{2} \varepsilon_{ijk} t^k \quad (\text{B.2})$$

are the symmetric and antisymmetric parts of the distortion tensor \mathbf{H} , and we have used the fact that \mathbf{t} is divergence-less. Note that the transverse or curl part of the displacement also contributes to the symmetric distortion tensor \mathbf{M} . In this appendix, all spatial derivatives are with respect to Lagrangian coordinates \mathbf{q} .

In the code implementation, we add the symmetric transverse contribution to \mathbf{M} in the first line of Eq. (B.2) at each order. It then remains to derive the contributions of the antisymmetric part \mathbf{C} to the distortion tensor.

For the longitudinal source, we have, first,

$$\text{tr}(\mathbf{H}^{(a)} \mathbf{H}^{(b)}) = \text{tr}(\mathbf{M}^{(a)} \mathbf{M}^{(b)}) + \text{tr}(\mathbf{C}^{(a)} \mathbf{C}^{(b)})$$

$$= \text{tr}(\mathbf{M}^{(a)} \mathbf{M}^{(b)}) + \frac{1}{2} \mathbf{t}^{(a)} \cdot \mathbf{t}^{(b)}, \quad (\text{B.3})$$

while $\text{tr}(\mathbf{C}) = 0$. Note that $\text{tr}(\mathbf{M}\mathbf{C})$ vanishes by symmetry as well. Second, the transverse contributions to the cubic source term are

$$\begin{aligned}
\varepsilon^{ijk} \varepsilon^{lmn} M_{il}^{(a)} M_{jm}^{(b)} M_{kn}^{(c)} \Big|_{\text{transverse}} &= \varepsilon^{ijk} \varepsilon^{lmn} M_{il}^{(a)} C_{jm}^{(b)} C_{kn}^{(c)} + 2 \text{ perm.} \\
&= \frac{1}{4} \varepsilon^{ijk} \varepsilon^{lmn} \varepsilon_{jmp} \varepsilon_{kno} M_{il}^{(a)} t^{(b)p} t^{(c)o} + 2 \text{ perm.} \\
&= \frac{1}{2} \mathbf{t}^{(b)\top} \cdot \mathbf{M}^{(a)} \cdot \mathbf{t}^{(c)} + 2 \text{ perm.} .
\end{aligned} \tag{B.4}$$

Again, the terms involving a single or three transverse components vanish by symmetry. Since \mathbf{t} starts at third order, the corresponding contributions to the longitudinal source terms start at sixth order.

Turning to the source terms for the transverse component, we have for the transverse contributions

$$\begin{aligned}
\varepsilon^{ijk} \left(\mathbf{H}^{(a)} \mathbf{H}^{(b)\top} \right)_{jk} \Big|_{\text{transverse}} &= \varepsilon^{ijk} \left(C_{jm}^{(a)} M_{mk}^{(b)} - M_{jm}^{(a)} C_{mk}^{(b)} - C_{jm}^{(a)} C_{mk}^{(b)} \right) \\
&= \frac{1}{2} \left(t^{(a)i} \text{tr}(\mathbf{M}^{(b)}) - t^{(b)i} \text{tr}(\mathbf{M}^{(a)}) + M_{im}^{(a)} t^{(b)m} - M_{im}^{(b)} t^{(a)m} \right) \\
&\quad + \frac{1}{4} \varepsilon^{ijk} t_j^{(a)} t_k^{(b)}.
\end{aligned} \tag{B.5}$$

Here, the leading contribution is at fourth order. However, since the transverse part of the displacement is always much smaller than the longitudinal part, the overall contribution to the source terms remains highly suppressed at least up to $n = 7$.

References

- [1] F. Schmidt, *Sigma-eight at the percent level: the EFT likelihood in real space*, *JCAP* **2021** (Apr., 2021) 032, [[2009.14176](#)].
- [2] M. Lippich, A. G. Sánchez, M. Colavincenzo, E. Sefusatti, P. Monaco, L. Blot et al., *Comparing approximate methods for mock catalogues and covariance matrices - I. Correlation function*, *MNRAS* **482** (Jan., 2019) 1786–1806, [[1806.09477](#)].
- [3] S. Tassev and M. Zaldarriaga, *The mildly non-linear regime of structure formation*, *JCAP* **2012** (Apr., 2012) 013, [[1109.4939](#)].
- [4] T. Baldauf, E. Schaan and M. Zaldarriaga, *On the reach of perturbative descriptions for dark matter displacement fields*, *JCAP* **2016** (Mar., 2016) 017, [[1505.07098](#)].
- [5] M. M. Abidi and T. Baldauf, *Cubic Halo Bias in Eulerian and Lagrangian Space*, *JCAP* **1807** (2018) 029, [[1802.07622](#)].
- [6] T. Lazeyras and F. Schmidt, *Beyond LIMD bias: a measurement of the complete set of third-order halo bias parameters*, *JCAP* **1809** (2018) 008, [[1712.07531](#)].
- [7] T. Steele and T. Baldauf, *Precise Calibration of the One-Loop Bispectrum in the Effective Field Theory of Large Scale Structure*, *arXiv e-prints* (Sept., 2020) arXiv:2009.01200, [[2009.01200](#)].
- [8] A. Taruya, T. Nishimichi and D. Jeong, *Grid-based calculation for perturbation theory of large-scale structure*, *Phys. Rev. D* **98** (2018) 103532, [[1807.04215](#)].
- [9] A. Taruya, T. Nishimichi and D. Jeong, *The covariance of the matter power spectrum including the survey window function effect: N-body simulations vs. fifth-order perturbation theory on grid*, *arXiv e-prints* (July, 2020) arXiv:2007.05504, [[2007.05504](#)].

- [10] J. Jasche and B. D. Wandelt, *Bayesian physical reconstruction of initial conditions from large-scale structure surveys*, *MNRAS* **432** (June, 2013) 894–913, [[1203.3639](#)].
- [11] M. Ata, F.-S. Kitaura and V. Müller, *Bayesian inference of cosmic density fields from non-linear, scale-dependent, and stochastic biased tracers*, *MNRAS* **446** (Feb., 2015) 4250–4259, [[1408.2566](#)].
- [12] U. Seljak, G. Aslanyan, Y. Feng and C. Modi, *Towards optimal extraction of cosmological information from nonlinear data*, *JCAP* **12** (Dec., 2017) 009, [[1706.06645](#)].
- [13] F. Elsner, F. Schmidt, J. Jasche, G. Lavaux and N.-M. Nguyen, *Cosmology Inference from Biased Tracers using the EFT-based Likelihood*, *JCAP* **2001** (2020) 029, [[1906.07143](#)].
- [14] G. Lavaux, J. Jasche and F. Leclercq, *Systematic-free inference of the cosmic matter density field from SDSS3-BOSS data*, *arXiv e-prints* (Sept., 2019) arXiv:1909.06396, [[1909.06396](#)].
- [15] F. Bernardeau, S. Colombi, E. Gaztanaga and R. Scoccimarro, *Large scale structure of the universe and cosmological perturbation theory*, *Phys.Rept.* **367** (2002) 1–248, [[astro-ph/0112551](#)].
- [16] V. Desjacques, D. Jeong and F. Schmidt, *Large-scale galaxy bias*, *PhR* **733** (Feb., 2018) 1–193, [[1611.09787](#)].
- [17] M. Schmittfull, M. Simonović, V. Assassi and M. Zaldarriaga, *Modeling Biased Tracers at the Field Level*, *Phys. Rev.* **D100** (2019) 043514, [[1811.10640](#)].
- [18] M. Schmittfull, M. Simonović, M. M. Ivanov, O. H. E. Philcox and M. Zaldarriaga, *Modeling Galaxies in Redshift Space at the Field Level*, *arXiv e-prints* (Dec., 2020) arXiv:2012.03334, [[2012.03334](#)].
- [19] T. Fujita and Z. Vlah, *Perturbative description of biased tracers using consistency relations of LSS*, *JCAP* **2020** (Oct., 2020) 059, [[2003.10114](#)].
- [20] Y. Donath and L. Senatore, *Biased tracers in redshift space in the EFTofLSS with exact time dependence*, *JCAP* **2020** (Oct., 2020) 039, [[2005.04805](#)].
- [21] T. Buchert, *Lagrangian theory of gravitational instability of Friedman-Lemaitre cosmologies and the 'Zel'dovich approximation'*, *MNRAS* **254** (Feb., 1992) 729–737.
- [22] T. Buchert, *Lagrangian Theory of Gravitational Instability of Friedman-Lemaitre Cosmologies - a Generic Third-Order Model for Nonlinear Clustering*, *MNRAS* **267** (Apr., 1994) 811, [[astro-ph/9309055](#)].
- [23] F. R. Bouchet, S. Colombi, E. Hivon and R. Juszkiewicz, *Perturbative Lagrangian approach to gravitational instability.*, *A&A* **296** (Apr., 1995) 575, [[astro-ph/9406013](#)].
- [24] P. Catelan, *Lagrangian dynamics in non-flat universes and non-linear gravitational evolution*, *MNRAS* **276** (Sept., 1995) 115–124, [[astro-ph/9406016](#)].
- [25] C. Rampf and T. Buchert, *Lagrangian perturbations and the matter bispectrum I: fourth-order model for non-linear clustering*, *JCAP* **2012** (June, 2012) 021, [[1203.4260](#)].
- [26] Z. Vlah, M. White and A. Aviles, *A Lagrangian effective field theory*, *JCAP* **2015** (Sept., 2015) 014, [[1506.05264](#)].
- [27] T. Matsubara, *Nonlinear perturbation theory with halo bias and redshift-space distortions via the Lagrangian picture*, *PhRvD* **78** (Oct., 2008) 083519, [[0807.1733](#)].
- [28] S.-F. Chen, Z. Vlah and M. White, *Consistent modeling of velocity statistics and redshift-space distortions in one-loop perturbation theory*, *JCAP* **2020** (July, 2020) 062, [[2005.00523](#)].
- [29] S. Tassev, *Lagrangian or Eulerian; real or Fourier? Not all approaches to large-scale structure are created equal*, *JCAP* **2014** (June, 2014) 008, [[1311.4884](#)].

- [30] M. Mirbabayi, F. Schmidt and M. Zaldarriaga, *Biased tracers and time evolution*, *JCAP* **7** (July, 2015) 030, [[1412.5169](#)].
- [31] G. Cabass, *The EFT Likelihood for Large-Scale Structure in Redshift Space*, [2007.14988](#).
- [32] G. Cabass and F. Schmidt, *The Likelihood for LSS: Stochasticity of Bias Coefficients at All Orders*, *JCAP* **07** (2020) 051, [[2004.00617](#)].
- [33] F. Schmidt, F. Elsner, J. Jasche, N. M. Nguyen and G. Lavaux, *A rigorous EFT-based forward model for large-scale structure*, *Journal of Cosmology and Astro-Particle Physics* **2019** (Jan, 2019) 042, [[1808.02002](#)].
- [34] F. Schmidt, G. Cabass, J. Jasche and G. Lavaux, *Unbiased cosmology inference from biased tracers using the EFT likelihood*, *JCAP* **2020** (Nov., 2020) 008, [[2004.06707](#)].
- [35] G. Cabass and F. Schmidt, *The EFT Likelihood for Large-Scale Structure*, *JCAP* **04** (2020) 042, [[1909.04022](#)].
- [36] D. Jeong and F. Schmidt, *Large-scale structure observables in general relativity*, *Classical and Quantum Gravity* **32** (Feb., 2015) 044001, [[1407.7979](#)].
- [37] C. Rampf, *The recursion relation in Lagrangian perturbation theory*, *JCAP* **12** (Dec., 2012) 4, [[1205.5274](#)].
- [38] V. Zheligovsky and U. Frisch, *Time-analyticity of Lagrangian particle trajectories in ideal fluid flow*, *Journal of Fluid Mechanics* **749** (June, 2014) 404–430, [[1312.6320](#)].
- [39] T. Matsubara, *Recursive solutions of Lagrangian perturbation theory*, *PhRvD* **92** (July, 2015) 023534, [[1505.01481](#)].
- [40] T. Buchert and J. Ehlers, *Averaging inhomogeneous Newtonian cosmologies.*, *A&A* **320** (Apr., 1997) 1–7, [[astro-ph/9510056](#)].
- [41] J. Ehlers and T. Buchert, *Newtonian Cosmology in Lagrangian Formulation: Foundations and Perturbation Theory*, *General Relativity and Gravitation* **29** (June, 1997) 733–764, [[astro-ph/9609036](#)].
- [42] M. Crocce, S. Pueblas and R. Scoccimarro, *Transients from initial conditions in cosmological simulations*, *MNRAS* **373** (Nov., 2006) 369–381, [[astro-ph/0606505](#)].
- [43] O. Hahn, M. Michaux, C. Rampf, C. Uhlemann and R. E. Angulo, *MUSIC2-monofonIC: 3LPT initial condition generator*, Aug., 2020.
- [44] C. Rampf and O. Hahn, *Shell-crossing in a Λ CDM Universe*, *arXiv e-prints* (Oct., 2020) arXiv:2010.12584, [[2010.12584](#)].
- [45] L. Senatore, *Bias in the effective field theory of large scale structures*, *JCAP* **11** (Nov., 2015) 007, [[1406.7843](#)].
- [46] T. Fujita, V. Mauerhofer, L. Senatore, Z. Vlah and R. Angulo, *Very massive tracers and higher derivative biases*, *JCAP* **2020** (Jan., 2020) 009, [[1609.00717](#)].
- [47] T. Lazeyras and F. Schmidt, *A robust measurement of the first higher-derivative bias of dark matter halos*, *arXiv e-prints* (Apr, 2019) arXiv:1904.11294, [[1904.11294](#)].
- [48] P. Coles and P. Erdogdu, *Scale dependent galaxy bias*, *JCAP* **2007** (Oct., 2007) 007, [[0706.0412](#)].
- [49] A. Pontzen, *Scale-dependent bias in the baryonic-acoustic-oscillation-scale intergalactic neutral hydrogen*, *PhRvD* **89** (Apr., 2014) 083010, [[1402.0506](#)].
- [50] G. Cabass and F. Schmidt, *A new scale in the bias expansion*, *JCAP* **2019** (May, 2019) 031, [[1812.02731](#)].
- [51] S. A. Orszag, *On the Elimination of Aliasing in Finite-Difference Schemes by Filtering High-Wavenumber Components.*, *Journal of Atmospheric Sciences* **28** (Sept., 1971) 1074–1074.

- [52] V. Springel, *The cosmological simulation code GADGET-2*, *MNRAS* **364** (Dec., 2005) 1105–1134, [[astro-ph/0505010](#)].
- [53] P. Coles, A. L. Melott and S. F. Shandarin, *Testing approximations for non-linear gravitational clustering*, *MNRAS* **260** (Feb., 1993) 765–776.
- [54] C. Rampf, B. Villone and U. Frisch, *How smooth are particle trajectories in a Λ CDM Universe?*, *MNRAS* **452** (Sept., 2015) 1421–1436, [[1504.00032](#)].
- [55] N. McCullagh, D. Jeong and A. S. Szalay, *Toward accurate modelling of the non-linear matter bispectrum: standard perturbation theory and transients from initial conditions*, *MNRAS* **455** (Jan., 2016) 2945–2958, [[1507.07824](#)].
- [56] T. Nishimichi et al., *Dark Quest. I. Fast and Accurate Emulation of Halo Clustering Statistics and Its Application to Galaxy Clustering*, *Astrophys. J.* **884** (2019) 29, [[1811.09504](#)].
- [57] M. Michaux, O. Hahn, C. Rampf and R. E. Angulo, *Accurate initial conditions for cosmological N-body simulations: Minimizing truncation and discreteness errors*, [2008.09588](#).
- [58] D. Baumann, A. Nicolis, L. Senatore and M. Zaldarriaga, *Cosmological non-linearities as an effective fluid*, *JCAP* **7** (July, 2012) 051, [[1004.2488](#)].
- [59] J. J. M. Carrasco, M. P. Hertzberg and L. Senatore, *The effective field theory of cosmological large scale structures*, *Journal of High Energy Physics* **9** (Sept., 2012) 82, [[1206.2926](#)].
- [60] S. M. Carroll, S. Leichenauer and J. Pollack, *Consistent effective theory of long-wavelength cosmological perturbations*, *Phys. Rev.* **D90** (2014) 023518, [[1310.2920](#)].
- [61] J. J. M. Carrasco, S. Foreman, D. Green and L. Senatore, *The 2-loop matter power spectrum and the IR-safe integrand*, *JCAP* **1407** (2014) 056, [[1304.4946](#)].
- [62] R. Angulo, M. Fasiello, L. Senatore and Z. Vlah, *On the Statistics of Biased Tracers in the Effective Field Theory of Large Scale Structures*, *JCAP* **1509** (2015) 029, [[1503.08826](#)].
- [63] T. Baldauf, L. Mercolli and M. Zaldarriaga, *Effective field theory of large scale structure at two loops: The apparent scale dependence of the speed of sound*, *Phys. Rev.* **D92** (2015) 123007, [[1507.02256](#)].
- [64] T. Buchert, A. L. Melott and A. G. Weiss, *Testing higher-order Lagrangian perturbation theory against numerical simulations I. Pancake models*, *A&A* **288** (Aug., 1994) 349–364, [[astro-ph/9309056](#)].
- [65] A. L. Melott, T. Buchert and A. G. Weiss, *Testing higher-order Lagrangian perturbation theory against numerical simulations. II. Hierarchical models.*, *A&A* **294** (Feb., 1995) 345–365, [[astro-ph/9404018](#)].
- [66] F. Schmidt, *Monodromic Dark Energy*, *arXiv e-prints* (Sept., 2017) arXiv:1709.01544, [[1709.01544](#)].
- [67] D. K. Ramanah, G. Lavaux, J. Jasche and B. D. Wandelt, *Cosmological inference from Bayesian forward modelling of deep galaxy redshift surveys*, *A&A* **621** (Jan, 2019) A69, [[1808.07496](#)].